44th AIAA Aerospace Sciences Meeting and Exhibit
9 - 12 January 2006, Reno, Nevada

AIAA 2006-154

Large-Eddy Simulation of Swirl-Stabilized Spray Combustion

Nayan Patel* and Suresh Menon†

School of Aerospace Engineering

Georgia Inst. of Technology, Atlanta, GA 30332.

Large-Eddy Simulation of swirl-stabilized flow in a laboratory combustor have been performed for non-reacting and reacting conditions and both gas- and liquid-phase results are compared with available data. Dynamic model is employed for momentum subgrid closure in this study. Additionally, simulations with two reaction rate closures are performed and compared. Results for non-reacting case show the presence of vortex breakdown bubble (VBB) in the center-line region with two corner recirculation zones past the dump plane. Non-reacting comparisons with measurements for both mean and RMS show good agreement. Reacting simulations show presence of stronger but smaller VBB in the center-line region. Overall, reacting comparisons with measurements are also in reasonable agreement. Time-averaged flow visualization in form of streamlines indicate that the non-reacting flow rotates twice as much from the inflow to outflow boundary than the reacting case. Droplet data show good agreement for particle velocity profiles and reasonable trends for the SMD variation.

I. Introduction

DESIGN and development of combustion devices has exclusively relied on empirical relations, past designs, and rig testing. Various external forces, like government regulations, market-demand, health & safety concerns, have presented a strong push[1] for cleaner burning combustion technology without sacrificing engine characteristics like high-thrust-to-weight ratios. Complexity of combustion device added with ever tightening pollution limits, has increasingly made the design process rely on physics-based combustion system calculations. Major impetus, according to recent article by Mongia,[2] is to develop *no-fudge factor* combustion design tools for achieving *pre-test prediction capability* which is equivalent to *running the engine*. The idea here is to assess the *impact* of the design on the overall operating engine characteristics,[2] like emissions, dome/liner wall temperature levels, pressure losses, profile and pattern factor, lean blowout and ignition, etc., without relying on emperical correlations or rig testing. For this idea to be fruitful, simulation of critical design effects with a reasonable (a week or less) turn-around time is essential. Besides aiding in design process, computational studies has potential for exploring fundamental physical phenomena[3] without added complexities of hardware and measurement uncertainties especially in operational configuration and conditions.

In the current study, we focus on a laboratory swirl-cup configuration being investigated by Colby *et al.*[4,5] Previous computational studies, mostly involving Reynolds Averaged Navier-Stokes (RANS) approach, on similar swirl-cup configuration have been performed. Tolpadi *et al.*[6] undertook RANS computations and validation of two-phase, non-reacting and isothermal, non-vaporizing, 2D-axisymmetric flow field for the single annular combustor. For the gas phase, the axisymmetric RANS calculations overpredicted mean profiles (for all three components) especially for the azimuthal (or tangential) component. Also, since the axisymmetric calculations were performed, both the radial and tangential computed profiles approached zero contrary to that seen in experiments. For the liquid phase, the data was compared at the next axial measurement location indicating fair agreement for axial and radial velocities for large to medium size (30-100 μm) droplets. The swirl component showed poor agreement due to axisymmetric assumption.

Hsiao *et al.*[7] had led efforts to assess/calibrate commercially available software – Fluent package – for non-reacting flow. Authors have advocated "through-the-vane"(TTV) approach for the swirl cup assembly

*Graduate Student; gte101g@mail.gatech.edu

†Professor, Associate Fellow; suresh.menon@ae.gatech.edu

to minimize uncertainty in specifying the inlet boundary conditions for the combustor. Comparisons for the axial velocity showed that peaks (both negative in the recirculation zone and positive in shear layer region) and their magnitude compared well at most axial locations however, the length of recirculation bubble was over-predicted. For the radial component, the comparisons were fair with some overpredictions in the shear-layer regions. Their simulations revealed a counter-rotating feature at the first measurement location (3 mm downstream of the flare exit) which is not seen in experiments. To address the turbulence model deficiencies, Hsiao *et al.*[8] set out to study the effect of five RANS turbulence models implemented in the commercially available Fluent package. The configuration used was a 90^o (periodic) sector volume with hybrid domain and compared with LDV non-reacting data.[9] The authors acknowledged that all five turbulence models predicted similar results.

Wang *et al.*[10] had undertaken investigation of non-reacting flow dynamics using Large-Eddy Simulation (LES) technique. The computational domain they used incorporated both the primary as well as the secondary swirler ejecting the flow field in a dump combustor. Various instantaneous snapshots of pressure and angular momentum were presented signifying the unsteady dynamics and their interactions however, no quantitative comparisons with experiments for flow characteristics were presented. In summary, their study gave a qualitative look into the capabilities of LES.

Recently, several studies of two-phase LES in a realistic full-scale gas turbine combustors have been carried out. Sankaran and Menon[11] investigated unsteady interactions between spray dispersion, vaporization, fuel-air mixing, and heat release in a realistic combustor. Results showed increase in droplet dispersion with swirl and large scale coherent structures are subjected to complex stretch effects in the presence of swirling motion. Menon and Patel[12] studied spray combustion under different operating conditions for twin burner configuration. They showed that shape of the combustor significantly impacts three-dimensional motions with no similarity between flame structures and vortex breakdown bubbles between the two burners. These studies gave qualitative look into the chemistry-turbulence interactions however, no measurement data were available for comparisons mainly due to realistic (typically 20-35 atmospheres and 800-1200K preheat) operating conditions.

This study aims to apply and investigate the ability of compressible LES approach to resolve processes for both non-reacting and reacting (spray) flow-field in a swirl-stabilized experimental combustor[4,5] operated at atmospheric pressure. The measurements are performed by Colby *et al.*[4,5] at Georgia Tech and will be used in this study for validation purposes. Due to significant differences in combustor configuration and operating conditions, no comparisons are made with previous[6–8] computational studies. Unique aspect of this study is the application of both Localized Dynamic K-equation Model (LDKM)[13,14] and the Linear Eddy Mixing (LEM)[12,15,16] model for achieving momentum and scalar equation closures, respectively. The combination results in a simulation approach that has no model parameters to adjust regardless of the physical problem simulated. Both the gas and liquid phase validations are reported and discussed.

II. Mathematical Formulation

The conservation equations for compressible reacting flow are solved using the Large-Eddy Simulation methodology in generalized co-ordinates. To simulate multiphase (spray) combustion, Lagrangian spray model is concurrently solved with Eulerian gas phase.

Eulerian-Phase LES Equations

Applying the filtering operation, using a low-pass box filter, to the instantaneous Navier-Stokes equations, the following filtered LES equations are obtained:

$$\begin{aligned}
\frac{\partial \bar{\rho}}{\partial t} &= \widetilde{\dot{\rho}_s} - \frac{\partial \bar{\rho}\tilde{u}_j}{\partial x_j} \\
\frac{\partial \bar{\rho}\tilde{u}_i}{\partial t} &= \widetilde{\dot{F}_{s,i}} - \frac{\partial}{\partial x_j}[\bar{\rho}\tilde{u}_i\tilde{u}_j + \bar{p}\delta_{ij} - \bar{\tau}_{ij} + \tau_{ij}^{sgs}] \\
\frac{\partial \bar{\rho}\tilde{E}}{\partial t} &= \widetilde{\dot{Q}_s} - \frac{\partial}{\partial x_i}[(\bar{\rho}\tilde{E} + \bar{p})\tilde{u}_i + \bar{q}_i - \tilde{u}_j\bar{\tau}_{ji} + H_i^{sgs} + \sigma_i^{sgs}] \\
\frac{\partial \bar{\rho}\tilde{Y}_k}{\partial t} &= \widetilde{\dot{S}_{s,k}} - \frac{\partial}{\partial x_i}[\bar{\rho}\tilde{Y}_k\tilde{u}_i + \bar{\rho}\tilde{Y}_k\widetilde{V_{i,k}} + Y_{i,k}^{sgs} + \theta_{i,k}^{sgs}] + \bar{\dot{w}}_k
\end{aligned} \tag{1}$$

where, $\overline{\rho}$ is filtered mass density, $\widetilde{u}_i$ is the resolved velocity vector, $\widetilde{Y_k}$ is the resolved species mass fraction, $\widetilde{V_{i,k}}$ is the resolved species diffusion velocity, $\overline{p}$ filtered pressure determined from filtered equation of state (shown later), $\widetilde{E}$ is resolved total energy per unit mass, $\overline{\tau_{ij}}$ is filtered viscous stress, and $\overline{q_i}$ is the heat flux vector. The sub-grid terms resulting from the filtering operation, denoted with super-script ^{sgs}, represent the small-scale effects upon the resolved-scales in the form of additional stresses and fluxes. Subscript s denote source terms from dispersed phase and index k for species varies from 1 to N_s, where N_s is the total number of species present in the system.

The viscous stress tensor ($\overline{\tau_{ij}}$) and heat flux vector ($\overline{q_i}$) are given as:

$$\begin{aligned}\overline{\tau_{ij}} &= \mu(\frac{\partial\widetilde{u}_i}{\partial x_j}+\frac{\partial\widetilde{u}_j}{\partial x_i})-\frac{2}{3}\mu(\frac{\partial\widetilde{u_k}}{\partial x_k})\delta_{ij}\\ \overline{q_i} &= -\overline{\kappa}\frac{\partial\widetilde{T}}{\partial x_i}+\bar{\rho}\sum_{k=1}^{N_s}\tilde{h}_k\tilde{Y}_k\widetilde{V_{i,k}}+\sum_{k=1}^{N_s}q_{i,k}^{sgs}\end{aligned}$$

where, the diffusion velocities are approximated using Fickian diffusion as $\widetilde{V_{i,k}} = (-\bar{D}_k/\tilde{Y}_k)(\partial\tilde{Y}_k/\partial x_i)$, molecular viscosity ($\mu$) is approximated by Sutherland's Law based on resolved temperature ($\widetilde{T}$), and the thermal conductivity ($\bar{\kappa}$) is approximated as $\bar{\kappa} = \mu\bar{C}_p/Pr$, where $\bar{C}_p$ is the specific heat at constant pressure for gaseous mixture and Pr is the Prandtl number.

The pressure is determined from the filtered equation of state,

$$\bar{p} = \bar{\rho}R_u\sum_{k=1}^{N_s}[\frac{\tilde{Y}_k\tilde{T}}{MW_k}+\frac{T_k^{sgs}}{MW_k}] \tag{2}$$

where, R_u and MW_k are the universal gas constant and $k-th$ species molecular weight, respectively. The subgrid temperature-species correlation term is defined as, $T_k^{sgs} = [\widetilde{Y_kT}-\tilde{Y}_k\tilde{T}]$.

The filtered total energy per unit volume is given by $\bar{\rho}\tilde{E} = \bar{\rho}\tilde{e}+\frac{1}{2}\bar{\rho}\tilde{u}_i\tilde{u}_i+\bar{\rho}k^{sgs}$ where, the sub-grid kinetic energy (discussed later) is defined as, $k^{sgs} = (1/2)[\widetilde{u_ku_k}-\tilde{u}_k\tilde{u}_k]$. The filtered specific internal energy is given by $\tilde{e} = \sum_{k=1}^{N_s}[\tilde{Y}_k\tilde{h}_k+(\widetilde{Y_kh_k}-\tilde{Y}_k\tilde{h_k})]-\bar{p}/\bar{\rho}$ where, $\widetilde{h_k} = \Delta h_{f,k}^o+\int_{T^o}^{\widetilde{T}}C_{p,k}(T')dT'$ is the specific enthalpy at filtered temperature ($\widetilde{T}$). For calorically perfect gas, the filtered specific internal energy equation simplifies to $\tilde{e} = \sum_{k=1}^{N_s}[c_{v,k}\tilde{Y}_k\tilde{T}+c_{v,k}T_k^{sgs}+\tilde{Y}_k\Delta h_{f,k}^{'}]$ where, $\Delta h_{f,k}^{'} = \Delta h_{f,k}^0-c_{p,k}T^0$ and $\Delta h_{f,k}^0$ is the standard heat of formation at a reference temperature T^0.

The SGS terms that require closure are: the sub-grid stress tensor, the sub-grid enthalpy flux, the sub-grid viscous work, the sub-grid convective species flux, the sub-grid heat flux, the sub-grid species diffusive flux, and the subgrid temperature-species correlation, respectively:

$$\begin{aligned}\tau_{ij}^{sgs} &= \overline{\rho}\,(\widetilde{u_iu_j}-\widetilde{u}_i\widetilde{u}_j)\\ H_i^{sgs} &= \overline{\rho}\,(\widetilde{Eu_i}-\widetilde{E}\widetilde{u}_i)+(\overline{pu_i}-\overline{p}\widetilde{u}_i)\\ \sigma_i^{sgs} &= \widetilde{u_j\tau_{ij}}-\widetilde{u}_j\overline{\tau}_{ij}\\ Y_{i,k}^{sgs} &= \bar{\rho}[\widetilde{u_iY_k}-\tilde{u}_i\tilde{Y}_k]\\ q_{i,k}^{sgs} &= [\overline{h_kD_k\partial Y_k/\partial x_i}-\tilde{h}_k\tilde{D}_k\partial\tilde{Y}_k/\partial x_i]\\ \theta_{i,k}^{sgs} &= \bar{\rho}[\widetilde{V_{i,k}Y_k}-\widetilde{V}_{i,k}\widetilde{Y}_k]\\ T_k^{sgs} &= \widetilde{Y_kT}-\tilde{Y}_k\tilde{T}\end{aligned} \tag{3}$$

The closure of these terms in addition to the closure for the filtered chemical reaction source terms ($\bar{\dot{w}}_k$) and the source terms for the dispersed phase in Eq. (1) are described below.

Momentum Transport Closure

The sub-grid stress tensor τ_{ij}^{sgs} is modeled as:

$$\tau_{ij}^{sgs} = -2\overline{\rho}\,\nu_t(\widetilde{S}_{ij}-\frac{1}{3}\widetilde{S}_{kk}\delta_{ij})+\frac{2}{3}\overline{\rho}k^{sgs}\delta_{ij} \tag{4}$$

where, resolved strain-rate is given as $\widetilde{S_{ij}} = (1/2)[\frac{\partial\widetilde{u_i}}{\partial x_j}+\frac{\partial\widetilde{u_j}}{\partial x_i}]$. The subgrid eddy viscosity is modeled as: $\nu_t = C_\nu(\sqrt{k^{sgs}})\overline{\Delta}$ where $\overline{\Delta} = (\Delta x\Delta y\Delta z)^{1/3}$ is based on local grid size $(\Delta x, \Delta y, \Delta z)$. A transport model for the subgrid kinetic energy (k^{sgs}) is also solved:[17–19]

$$\frac{\partial \overline{\rho}\, k^{sgs}}{\partial t} + \frac{\partial}{\partial x_i}\left(\overline{\rho}\, \widetilde{u}_i k^{sgs}\right) = P^{sgs} - D^{sgs} + \frac{\partial}{\partial x_i}\left(\overline{\rho}\, \frac{\nu_t}{\sigma_k} \frac{\partial k^{sgs}}{\partial x_i}\right) + F_d \tag{5}$$

where, σ_k is a model constant typically equal to unity. Here, $P^{sgs} = -\tau_{ij}^{sgs}(\partial \widetilde{u}_i/\partial x_j)$ and $D^{sgs} = C_\varepsilon \overline{\rho}(k^{sgs})^{3/2}/\overline{\Delta}$ are, respectively, the production and the dissipation of k^{sgs}. In the above equation, $F_d = \widetilde{u_i F_{s,i}} - \widetilde{u}_i \widetilde{F_{s,i}}$ is the source term due to the particle phase (this term can be closed exactly, as shown earlier[20]).

The two coefficients in this model, C_ν and C_ε are obtained dynamically as a part of the solution using a localized dynamic technique (LDKM).[18,19,21] Fully localized evaluation of these coefficients in space and time is achieved in this approach. The nominal "constant" values for these coefficients are[22,23] 0.067 and 0.916, respectively. The dynamic procedure uses the experimental observation in high Re turbulent jet[24] that the subgrid stress τ_{ij}^{sgs} at the grid filter level $\overline{\Delta}$ and the Leonard's stress $L_{ij}(= [\langle \overline{\rho} \widetilde{u_i} \widetilde{u_j} \rangle - \frac{\langle \overline{\rho} \widetilde{u_i} \rangle \langle \widetilde{\overline{\rho} u_j} \rangle]}{\widehat{\overline{\rho}}})$ at the test filter level $\widehat{\Delta}(= 2\overline{\Delta})$ are self-similar. Here (and henceforth), $< f >$ and $\widehat{f}$ both indicate test filtering. Since L_{ij} can be explicitly computed at the test filter level, a simple scale-similar model of the form $\tau_{ij}^{sgs} = C_L L_{ij}$, where C_L is an adjustable constant, was proposed earlier[24] but was found to lack proper dissipation.

In the LDKM model, the above observation is extended and it is assumed that L_{ij} and the subgrid stress $\widehat{\tau}_{ij}^{sgs}$ at the test filter level are also similar (i.e., $\widehat{\tau}_{ij}^{sgs} = \widehat{C_L} L_{ij}$). Using this, $\widehat{\tau}_{ij}^{sgs}$ is modeled using the same form as for τ_{ij}^{sgs} (Eqn. 4), except that all variables are defined at the test filter level. We define the subgrid kinetic energy at the test filter level as $k_{test} = \frac{1}{2}[\frac{\widehat{\widetilde{\overline{\rho} u_k}^2}}{\widehat{\overline{\rho}}} - \frac{\widehat{\widetilde{\overline{\rho} u_k}}^2}{\widehat{\overline{\rho}}^2}]$ and obtain a relation

$$L_{ij} = \frac{\widehat{\tau}_{ij}^{sgs}}{\widehat{C_L}} = \frac{1}{\widehat{C_L}}[-2\widehat{\overline{\rho}} C_\nu \sqrt{k_{test}} \widehat{\Delta}(\langle \tilde{S_{ij}} \rangle - \frac{1}{3}\langle \tilde{S_{kk}} \rangle \delta_{ij}) + \frac{2}{3}\widehat{\overline{\rho}}\, k_{test} \delta_{ij}] \tag{6}$$

In the above equation, we assume $\widehat{C_L} = 1$ and so, the only unknown is C_ν. This equation is, thus, an explicit model representation for the constant C_ν in terms of quantities resolved at the test filter level. This system of equations represents five independent equations for one unknown coefficient (and hence, is an over-determined system). The value of C_ν is determined in an approximated manner by applying the least-square method.[25] Thus,

$$C_\nu = -\frac{L'_{ij} M_{ij}}{2 M_{ij} M_{ij}} \tag{7}$$

In the above expression

$$L'_{ij} = L_{ij} - \frac{2}{3}\widehat{\overline{\rho}}\, k_{test} \delta_{ij} \tag{8}$$

$$M_{ij} = \widehat{\overline{\rho}}\, \sqrt{k_{test}} \widehat{\Delta}(\langle \tilde{S_{ij}} \rangle - \frac{1}{3}\langle \tilde{S_{kk}} \rangle \delta_{ij}) \tag{9}$$

A similar approach is used to obtain the dissipation coefficient C_ε such that:

$$C_\epsilon = \frac{\widehat{\Delta}(\mu + \mu_t)}{\widehat{\overline{\rho}}\, k_{test}^{3/2}}[\langle \widetilde{T_{ij}} \frac{\partial \widetilde{u_j}}{\partial x_i} \rangle - \widehat{\widetilde{T_{ij}}} \frac{\widehat{\partial \widetilde{u_j}}}{\partial x_i}] \tag{10}$$

where μ is the molecular viscosity and $\mu_t(= \nu_t * \overline{\rho})$ is eddy viscosity at the grid filter level. The tensor $\widetilde{T_{ij}}$ is defined as $[\frac{\partial \widetilde{u_i}}{\partial x_j} + \frac{\partial \widetilde{u_j}}{\partial x_i} - \frac{2}{3}\frac{\partial \widetilde{u_k}}{\partial x_k}\delta_{ij}]$ and $\widehat{\widetilde{T_{ij}}}$ indicates tensor at the test-filter level.

Salient[12,26] aspects, among others, of the LDKM approach are: (a) the LDKM approach does not employ the Germano's identity,[27] (b) the self-similar approach implies that both $\overline{\Delta}$ and $\widehat{\Delta}$ must lie in the inertial range, and this provides a (albeit) rough estimate for the minimum grid resolution that can be used for a given Re, (c) the evaluation of the coefficients can be carried out locally (i.e., at all grid points) in space without encountering any instability, and (d) the LDKM approach satisfies all the realizability conditions[28] in the majority of the grid points even in complex swirling reacting flows.

Energy and Scalar Transport Closure

The subgrid total enthalpy flux, H_i^{sgs} is modeled using the eddy viscosity and a gradient assumption as:

$$H_i^{sgs} = -\overline{\rho}\frac{\nu_t}{Pr_t}\frac{\partial \widetilde{H}}{\partial x_i} \tag{11}$$

Here, $\widetilde{H}$ is the filtered total enthalpy and Pr_t is a turbulent Prandtl number that can also be computed using a dynamic procedure but is currently assumed to be unity. The total enthalpy term $\widetilde{H}$ is evaluated as sum of specific enthalpy of mixture, specific kinetic energy, and specific sub-grid scale energy: $\widetilde{H} = \widetilde{h} + \frac{\tilde{u}_i \tilde{u}_i}{2} + k^{sgs}$, where $\widetilde{h} = \sum_{k=1}^{N_s} \widetilde{h}_k \widetilde{Y}_k$.

In conventional LES (i.e., methods that solve the filtered species equations seen in Eqn. (1) along with the filtered Navier-Stokes equations), the subgrid convective species flux $Y_{i,k}^{sgs}$ is modeled using the gradient diffusion assumption, as well. This is used for scalar closure in eddy-breakup simulations. Thus,

$$Y_{i,k}^{sgs} = -\frac{\overline{\rho}\nu_t}{Sc_t}\frac{\partial \tilde{Y}_k}{\partial x_i} \tag{12}$$

The coefficient Sc_t is the turbulent Schmidt Number, and is taken to be unity but could be computed dynamically. The gradient closure for the species subgrid flux is more problematic than for momentum or energy transport, since scalar mixing and diffusion occur at the subgrid scale.

The other terms such as σ_i^{sgs}, $q_{i,k}^{sgs}$, $\theta_{i,k}^{sgs}$,and T_k^{sgs} are neglected[29] at present, but there is no clear justification.

Subgrid Scalar Closure in LEM

In the LEM model,[30–32] the filtered scalar equation shown in Eqn. (1) is not solved directly. Rather, molecular diffusion, small- and large-scale turbulent convection, and chemical reaction are all modeled separately, but concurrently at their respective time scales. To describe this model mathematically, we split the velocity field as: $u_i = \tilde{u}_i + (u_i')^R + (u_i')^S$. Here, $\tilde{u}_i$ is the LES-resolved velocity field, $(u_i')^R$ is the LES-resolved subgrid fluctuation (obtained from k^{sgs}) and $(u_i')^S$ is the unresolved subgrid fluctuation. Then, consider the *exact* species equation (i.e., without any explicit LES filtering) for the k-th scalar Y_k written in a slightly different form as:

$$\rho\frac{\partial Y_k}{\partial t} = -\rho[\tilde{u}_i + (u_i')^R + (u_i')^S]\frac{\partial Y_k}{\partial x_i} - \frac{\partial}{\partial x_i}(\rho Y_k V_{i,k}) + \dot{w}_k + \dot{S}_{s,k} \tag{13}$$

Implementation of LEM model in LES approach is called LEMLES, hereafter. In LEMLES, the above equation is rewritten as:

$$\frac{{Y_k}^* - {Y_k}^n}{\Delta t_{LES}} = -[\tilde{u}_i + (u_i')^R]\frac{\partial {Y_k}^n}{\partial x_i} \tag{14}$$

$${Y_k}^{n+1} - {Y_k}^* = \int_t^{t+\Delta t_{LES}} -\frac{1}{\rho}[\rho(u_i')^S\frac{\partial {Y_k}^n}{\partial x_i} + \frac{\partial}{\partial x_i}(\rho Y_k V_{i,k})^n - \dot{w}_k^n - \dot{S}_{s,k}^n]dt' \tag{15}$$

Here, Δt_{LES} is the LES time-step. Equation (14) describes the large-scale 3D LES-resolved convection of the scalar field, and is implemented by a Lagrangian transfer of mass across the finite-volume cell surfaces.[22,33] Equation (15) describes the subgrid LEM model, as viewed at the LES space and time scales. The integrand includes four processes that occur within each LES grid, and represent, respectively, (i) subgrid molecular diffusion, (ii) reaction kinetics, (iii) subgrid stirring, and (iv) phase change of the liquid fuel. These processes are modeled on a 1D domain embedded inside each LES grid where the integrand is rewritten in terms of the subgrid time and space scales. Descriptions for the subgrid processes (in Eq. (15)) and the 3D advection process (in Eq. (14)) are presented at length in Menon and Patel[12] and are omitted here, for brevity.

Since all the turbulent scales below the grid are resolved in this approach, both molecular diffusion and chemical kinetics are closed in an exact manner. As a result, "subgrid" terms such as $Y_{i,k}^{sgs}$, $q_{i,k}^{sgs}$, $\theta_{i,k}^{sgs}$, T_k^{sgs}, and $\bar{\dot{w}}_k$ do not have to be closed or modeled.

The LEM subgrid closure is similar to the closure in PDF methods[34] except that molecular diffusion is also included exactly in LEMLES in addition to finite-rate kinetics ($\dot{w}_k$). As in PDF methods, the large-scale transport is modeled as a Lagrangian transport of the scalar fields across LES cells, and the subgrid stirring is modeled. In PDF methods, a mixing model is often employed to model turbulent mixing, whereas, in LEMLES, small-scale turbulent stirring is implemented by the triplet mapping process.

Conservation of mass, momentum and energy (at the LES level) and conservation of mass, energy and species (at the LEM level) are fully coupled. Chemical reaction at the LEM level determines heat release and thermal expansion at the LEM level, which at the LES level generates flow motion that, in turns, transports the species field at the LEM level. Full coupling is maintained in the LEMLES to ensure local mass conservation.

Liquid-Phase Equations

The Lagrangian equation of motion governing instantaneous droplet, under the assumptions of dispersed droplet field leading to infrequent particle collisions and the Kolmogorov scale is of the same order or larger than the largest droplet, can be expressed as:[35,36]

$$\begin{aligned} \frac{dx_{i,p}}{dt} &= u_{i,p} \\ \frac{du_{i,p}}{dt} &= \frac{f}{\tau_V}(u_i - u_{i,p}) + g_i \end{aligned} \tag{16}$$

where, $u_{i,p}$ is the i-th component of the parcel velocity, u_i is the i-th component of gas-phase velocity, $x_{i,p}$ is the i-th component of parcel position, f is the *drag factor* (ratio of the drag coefficient to Stokes drag), τ_V is the particle velocity response time, and g_i is the i-th gravity component. Subscript p represents liquid phase quantities and unsubscribed quantities correspond to gas-phase (except as noted). Here, $u_i(=\widetilde{u_i}+u_i'')$ represent instantaneous gas-phase velocity components, consisting of both the LES resolved velocity $\widetilde{u_i}$ and a stochastic term u_i'' that is obtained using k^{sgs} at intervals coincident with the local characteristic eddy lifetime. Interaction of droplet with an eddy is assumed for a time taken as the smaller of either eddy lifetime or the transit time required to traverse the eddy. The drag factor and particle velocity response time are:

$$f = \frac{C_D Re_d}{24} \tag{17}$$

$$\tau_V = \frac{\rho_p d_p^2}{18\mu_g} \tag{18}$$

where, ρ_p is the liquid density, d_p is the parcel diameter ($= 2r_p$, r_p is parcel radius), μ_g is gas-phase dynamic viscosity, ν_g is gas-phase kinematic viscosity (μ_g/ρ_g), C_D is the drag coefficient, and Re_d is the relative particle Reynolds number expressed as $Re_d = (d_p/\nu_g)\sqrt{(u_i - u_{i,p})(u_i - u_{i,p})}$.

The drag coefficient accounts for the dynamic influence of pressure and viscous forces acting on droplet surfaces. Following,[37] the standard drag coefficient (assuming drops retain the spherical shape) is given by:

$$C_D = \begin{cases} \frac{24}{Re_d}(1 + \frac{1}{6}Re_d^{2/3}) & Re_d \leq 1000 \\ 0.4392 & Re_d > 1000 \end{cases} \tag{19}$$

The effect of droplet distortion on the drag coefficient can be accounted for in the breakup model.

The droplet mass transfer is governed by the droplet continuity equation,

$$\frac{dm_p}{dt} = -\dot{m}_p \tag{20}$$

where, m_p is the mass of particle given by $\frac{4}{3}\rho_p \pi r_p^3$, and $\dot{m}_p(> 0)$ is the net mass transfer rate (or vaporization rate) for a droplet in a convective flow field can be expressed[35] as:

$$\frac{\dot{m}_p}{\dot{m}_{p,Re_{d=0}}} = 1 + \frac{0.278\sqrt{Re_d}Sc^{(1/3)}}{[1 + \frac{1.232}{Re_d Sc^{(4/3)}}]^{(1/2)}} \tag{21}$$

where, $Re_{d=0}$ is the Reynolds number for particle at rest. Under quiescent conditions, the mass transfer rate reduces to:

$$\dot{m}_{p,Re_{d=0}} = 2\pi\rho_s \mathscr{D}_{sm} d_p ln(1 + B_M) \tag{22}$$

where, ρ_s and $\mathscr{D}_{sm}$ respectively, are the gas mixture density and the mixture diffusion coefficient at the droplet surface. Also, B_M is the Spalding transfer number[38] given by:

$$B_M \equiv b_\infty - b_s = \frac{(Y_{F,s} - Y_{F,\infty})}{(1 - Y_{F,s})}; \quad where\ b \equiv \frac{Y_F}{Y_{F,s} - 1}$$

In above relations, Sc ($\equiv \nu_{g,s}/\mathscr{D}_{sm}$, ratio of momentum to mass transport) is the Schmidt number. Subscript s represents quantities at droplet surface. Also, Y_F is the fuel species (that is evaporating) mass fraction. The mole fraction ($X_{F,s}$) at the droplet surface is obtained from Raoult's Law,[39] which assumes that the mole fraction at the droplet surface is equal to the ratio of the partial pressure of fuel vapor (P_{vap}) to the total pressure of gas-phase (P). Various correlations exist[40] to evaluate the partial pressure of fuel vapor that are typically specific for particular fuels and dependent on critical temperature and pressure of fuel

vapor. Droplet heat transfer is governed by the droplet energy equation, which consists of external and the internal energy, as well as, the energy associated with surface tension. The equation governing the internal temperature distribution based on this uniform temperature model[35,38] is:

$$m_p C_l \frac{dT_p}{dt} = \dot{Q}_{conv} - \dot{m}_p \mathscr{L}_v = h_p \pi d_p^2 (T - T_p) - \dot{m}_p \mathscr{L}_v \tag{23}$$

where, $\dot{Q_{conv}}$ is the convective thermal energy transfer rate, m_p is particle mass, C_l is liquid heat capacity, h_p is the heat transfer coefficient, and $\mathscr{L}_v$ is the latent heat of vaporization. Additional details of this model, including the heat transfer coefficient, are given elsewhere.[35,38]

Equations (16, 20, 23) are integrated using a fourth-order Runge-Kutta scheme. The integration is carried out based on the smallest of the time scales[35,41] (i.e., the smallest of the particle velocity relaxation time, the droplet life-time, the turbulent eddy interaction time, the droplet surface temperature constraint time, and the LES gas-phase CFL time) governing the particle evolution.

Eulerian-Lagrangian Coupling

Eulerian-Lagrangian coupling is through the inter-phase exchange terms[35] (not presented here, for brevity). If n_p number of particles are present per parcel/group, then the volume-averaged source terms for all the droplet parcel/group trajectories that cross a computational cell (of volume ΔV) are computed by summing the contribution from every parcel/group as follows:

$$\begin{pmatrix} \widetilde{\dot{\rho}_s} \\ \widetilde{\dot{F}_{s,i}} \\ \widetilde{\dot{Q}_s} \\ \widetilde{\dot{S}_{s,k}} \end{pmatrix} = \frac{1}{\Delta V} \begin{pmatrix} \sum_m n_p[\dot{m}_p] \\ \sum_m n_p[\dot{m}_p u_{i,p} - \frac{4\pi}{3}\rho_p r_p^3 \frac{du_{i,p}}{dt}] \\ \sum_m n_p[\dot{m}_p h_{v,s} - h_p \pi d_p^2 (T - T_p) - u_{i,p} m_p \frac{du_{i,p}}{dt} + \dot{m}_p(\frac{1}{2}u_{i,p}^2)] \\ \sum_m n_p[\dot{m}_p] \end{pmatrix}$$

where, the summation index "m" is over all the droplet parcels/groups crossing a computational cell (of volume ΔV). Also, note that the species source term ($\widetilde{\dot{S}_{s,k}}$) for all species ($k$) is *zero*, except for the species that is present in liquid form and evaporating.

Combustion Modeling

In this study, we have employed liquid fuel ($C_{12}H_{23}$) to approximate experimental Jet-A fuel. A three step, seven-species, global reduced mechanism[42,43] of the form:

$$C_{12}H_{23} + (35/2)O_2 \longrightarrow 12CO + (23/2)H_2O$$
$$2CO + O_2 \longrightarrow 2CO_2 \quad and \quad N_2 + O_2 \longrightarrow 2NO$$

is employed in this study. Global heat release effects and pollutant(CO and NO) distribution in the combustor can be investigated by this reduced mechanism, although with certain limitations.

The closure for the reaction rate is particularly important since it strongly impacts the LES prediction. LES closure for $\bar{\dot{w}_k}$ employed in EBULES is a conventional approach that utilizes a subgrid eddy break-up model.[44] In this model the filtered reaction rate ($\bar{\dot{w}_k}$) is computed as the minimum of the kinetic reaction rate and the mixing rate. For a general reaction mechanism comprising of N_r reactions given by $\sum_{k=1}^{N_s} \nu'_{k,j} M_{k,j} \rightleftharpoons \sum_{k=1}^{N_s} \nu"_{k,j} M_{k,j}$ the filtered reaction rates for species "k" is computed as follows $\bar{\dot{w}}_k = W_k \sum_{j=1}^{N_r} i(\nu"_{k,j} - \nu'_{k,j})\ \min[q_j^{mix}, q_j^{kin}]$ where q_j^{mix} and q_j^{kin} are the molar reaction rates based on mixing and Arrhenius chemical kinetic rate, respectively. The Arrhenius reaction rates for step "j" is given by, $q_j^{kin} = k_{f,j} \prod_{k=1}^{N_s} [M_k]_{k,j}^{\nu"} - k_{b,j} \prod_{k=1}^{N_s} [M_k]_{k,j}^{\nu'}$ and the mixing rates for the forward and the backward reactions are given by

$$q_{j,f}^{mix} = \frac{1}{\tau_M} \min\left(\frac{[M_k]}{\nu"_{k,j}}\right) \quad \text{and} \quad q_{j,b}^{mix} = \frac{1}{\tau_M} \min\left(\frac{[M_k]}{\nu'_{k,j}}\right) \tag{24}$$

Here, τ_M is the mixing time scale and is related to the sub-grid turbulence as follows $\tau_M = C_{EBU} \frac{\overline{\Delta}}{\sqrt{k^{sgs}}}$, with $C_{EBU} = 1$. In this study, subgrid kinetic energy (k^{sgs}) is evaluated dynamically and therefore, the reaction rate closure is dynamic as well. The proportionality constant is chosen as unity[44] for these studies. The chemical rate is based on Arrhenius kinetic rate adapted from Westbrook & Dryer[42] for the first two steps, and from Malte *et al.*[43] for the NO mechanism. In constrast, LEMLES approach does not require a closure for reaction rate as the instantanous species transport equation is solved directly without resorting to filtering.

III. Experimental Setup

The experimental study by Colby *et al.*[4,5] used a laboratory scale combustor with a trapezoidal cross-section having two windows on the sides for optical access. The main chamber converges gradually leading to a smaller trapezoidal cross-section for the purposes of flow acceleration to attain positive (out of the combustor) axial velocity. The swirl cup burner is an assembly of co-axial, counter-rotating airflows aided by eight-jet primary and ten-vaned secondary swirlers. The measurements, non-reacting and reacting, are performed at atmospheric conditions with nominal (379K) pre-heat air. Issues relevant to experimental set-up and measurement methods are described in Colby *et al.*[4,5] The case relevant to this study involved total mass (air) flow rate of 30.5 g/s and fuel mass flow rate of 0.750 g/s. For these flow conditions, the overall equivalence ratio amounted to 0.40.

IV. Numerical Method

For this study, we employ a compressible LES solver based on finite-volume scheme that is nominally second-order accurate in space and time. The solver has been implemented on a parallel processing environment using Message-Passing Interface (MPI) technique and scalability studies[45] performed.

Grid and Inflow Conditions

Figure 1 shows schematically the combustor domain used in the study, along with the grid distribution (every other node is shown). It also shows positions (at intersection of marked lines) of probes where transient signals are collected for spectral analysis. We have employed a two-domain, butterfly grid to resolve the central core of the combustor using a Cartesian grid (185×21×21) while a body-conforming cylindrical grid (185×74×81) is employed elsewhere. The combustor length from the dump plane ($x/R_o = 0.0$, equivalent to flare exit plane) to the exit is 0.278 m, the height is 0.0896 m, and the width is 0.0737 m (lower) and 0.103 m (upper). The circular inlet diameter ($D_o = 2R_o$) at the dump plane is 0.04026 m and the actual inlet is approximately $0.77R_o$ upstream of the dump plane. The swirl vanes and the internal details have not been modeled in the this study and therefore, the inflow velocity profiles, as shown in Fig. 2(a), at the computational inlet are considered approximate. Velocity profiles shown are non-dimensionalized by the bulk flow velocity ($U_o = 45.9$m/s). Hashed sections seen in the plot represent wall-surfaces present in the inflow plane. A bluff-body of $0.19R_o$ radius with origin at $r/R_o = 0.0$ is placed in the inlet section spanning $x = 0.08R_o$ axial distance from the inlet plane to represent constriction formed by the fuel injector.

Nominal conditions of atmospheric pressure and 379K pre-heat, the Reynolds number, $Re_D = U_0 D_0/\nu$ is 76,212 for the combustor. At the dump plane, using the computed k^{sgs} to estimate the subgrid velocity fluctuation u', and an integral length scale, $l \approx 0.65D_0$, the turbulence Reynolds number $Re_l = u'l/\nu$ is estimated around 9,800 and 17,446 for non-reacting and reacting cases, respectively. The corresponding subgrid Reynolds number, $Re_{\overline{\Delta}} = u'\overline{\Delta}/\nu$ is 113 and 187, respectively. Using scaling relations, the Kolmogorov scale η is 0.009 mm and 0.006 mm, respectively for the two cases in the high turbulence region. Analysis of the local values of $Re_{\overline{\Delta}}$ suggest that, in general, subgrid resolution used in LEMLES resolves around 2-4η in the regions of interest. Thus, the current resolution used for LEMLES is considered quite adequate.

Spray is injected using a Stochastic Separated Flow (SSF) approach[36] using parcels to represent groups of droplets with similar properties. Typically, around 25,000 to 35,000 droplet parcels (with 1-12 particles per group, chosen based on their size distribution function) are present, on an average. A log-normal size distribution, as shown in Fig. 2(b), with a Sauter-Mean Diameter (SMD) of 31.2 micron is used with a droplet cutoff radius (amounting to complete evaporation) of 4 μm. The particles are given initial momentum such that they form a hollow-cone pattern (consistent with the measurements). The location of particle injection is along the outer periphery of the center-bluff body (mentioned above) approximately $1mm$ downstream of the inflow plane.

Characteristics boundary conditions following Poinsot & Lele[46] are employed at the inflow and outflow planes. Adiabatic no-slip conditions are employed at all surface walls. Grid clustering is employed in regions of shear-layers and high-gradients along with nominal (5-8%) grid stretching in streamwise and radial directions. The minimum resolution in the inlet shear layer region is around 0.3 mm in the axial direction, 0.26 mm in the radial direction and 0.25 mm in the azimuthal direction. With this resolution, nearly 8-16 points are in the shear layer width, which is considered adequate. Figure 3 shows kinetic energy spectrum for both non-reacting and reacting cases at $(x/R_o, r/R_o)$=(0.0, 0.308) probe location. It can be seen that the current grid resolution is able to recover inertial range (as represented by the $-5/3$ slope) for

both the cases.

Time-step restriction for two-phase flow

There are many time-steps of importance in this type of problem. In addition to the usual LES time-step (Δt_{LES}), subgrid processes in LEMLES have additional time-steps for (a) reaction-diffusion (Δt_{LEM}), (b) subgrid stirring (Δt_{stir}), and (c) large-scale advection (Δt_{sp}). The LES time step, Δt_{LES} is the explicit time step determined by stability consideration. To maintain strict mass conservation, $\Delta t_{sp} = \Delta t_{LES}$. Δt_{stir} is determined from the stirring frequency,[12] λ, and Δt_{LEM} is determined by the minimum of the chemical and diffusion time within each cell needed for stable integration of the LEM equation.[12]

Inclusion of spray introduces more time scales in the flow. To accurately calculate the particle trajectories, size and temperature, the Lagrangian time step used for the integration has to be the smallest of the various physical time scales. The various time scales are: (1) Δt_{LES}, (2) the droplet velocity relaxation time, (3) the droplet life time, (4) the turbulent eddy droplet interaction time, and (5) the droplet surface temperature constraint time. At any instant, the smallest of the time scales is used for particle evolution[36] .

Computational Issues

Simulations are carried out using a parallel solver on a SGI Altix 3700 Linux cluster. For a single characteristic time τ (based on D_o and U_o), around 23 and 52 single-processor hours are needed for non-reacting and EBULES cases, respectively. After the initial transients, approximately 32τ and 26τ of data is statistically averaged for non-reacting and EBULES cases, respectively. For the LEMLES simulations, the processing cost is approximately seven times the EBULES. Although LEMLES is expensive, due to the high parallel scalability of the solver the turn-around time can be reduced by using a larger number of processors.

V. Results and Discussion

Results for the non-reacting and reacting simulations are presented in the following sub-sections.

A. Non-Reacting Simulation

Inflow velocity boundary conditions in this study have been approximated by a series of simulations initially conducted to determine sensitivity of the predictions (especially the centerline axial velocity) to the specified inflow profiles. Representative results were presented in Menon and Patel.[12] It was concluded that once axial and azimuthal profiles were determined based on bulk flow and swirl conditions, small variations in the radial component impacted the near field however, the far field remained relatively insensitive. In this study, both the non-reacting and reacting cases use the same inflow velocity profile.

Figure 4 the shows time-averaged streamwise velocity along the centerline of the combustor for both non-reacting and reacting (discussed in the next section) simulations. The profile is non-dimensionalized by the bulk flow velocity. For the non-reacting case, the axial velocity is consistently negative all the way to $x/R_o = 7.0$, indicating the length of the recirculation bubble. The peak negative axial velocity in the bubble is around $0.25U_o$, and the axial velocity is seen to gradually increase till it reaches the outflow boundary. Both the strength as well as the extent of the recirculation region is well predicted by the LES simulations. It can also be noted that the reverse region extends all the way into the inlet pipe consistent with the measurements.

Figure 5(a) show the streamlines and VBB region for the non-reacting simulation. It can be seen that the bubble is a single contiguous region and the flow swirls into and around the VBB. The swirl effect only weakens near the outflow and the flow is primarily axial by the time the outflow is reached. Analysis of the time evolution of the solution shows that the VBB is not stationary and oscillates in the axial direction with very small lateral movement. The mean flow rotates whole 2π from the inflow plane to the outflow boundary as seen by the streamlines. The sense of rotation is clockwise when viewed from the outflow boundary and is in the same sense as the outer/secondary swirler. Figure 5(b) shows the time-averaged streamwise velocity contour plot in the $x-y$ center plane. The resulting cross-sectional shape of the VBB resembles a leaf with its stem originating at the center-body located in the inlet pipe. No separation is observed at the 45^o flare expansion angle just upstream of the dump plane. The flow is seen to move parallel to the inlet wall and gradually decelerating before it impinges on the outer combustor wall at around $x/R_o = 2.0$.

Figures 6(a,c) show the normalized mean axial velocity profiles in the combustor at various axial locations. Two center planes are shown: horizontal $x-z$ plane (Fig. 6(a)) and a vertical $x-y$ plane (Fig. 6(c)). The

experimental data obtained at some of the axial locations are also shown. At the first location where data is available for comparison, both the peak value as well as the peak location in the shear layer region is well predicted. The strength of the reverse flow in the recirculation regions is also consistent with measurements. The reverse flow region is seen to spread (in radial direction) around $x/R_o = 2.3$ with peak values moving farther away from the centerline. Moving further downstream, the VBB quick diminishes in the radial direction and finally terminating around $x/R_o = 7.0$ (as seen in Fig. 4). The comparison with measurements at all downstream locations are in very good agreement for both the center-planes.

Figures 6(b) and 6(d) show respectively, the normalized mean azimuthal velocity profiles in the $x - z$ horizontal center-plane and the radial velocity profiles in the $x - y$ vertical center-plane at various axial locations. For these normal components, both the peak magnitude as well as peak locations in the shear layer regions are well predicted. Peak location of radial velocity and its rapid decay in axial direction indicates the effect of the 45^o flare angle. It was observed in a prior study (not presented here) that the effect of reducing the flare angle was to bring the peak location closer to the center-line. It can also be seen that the intensity of the azimuthal velocity is weaker in relation to the radial or axial components however, its decay is not as significant as seen for the radial component. Also, the presence of non-zero variation of azimuthal velocity along various axial locations indicate swirling flow in the combustor. This was seen before in form of swirling streamlines. The weaker intensity seen for azimuthal velocity is contributed to its transition to other two velocity components.

Comparisons for turbulence properties such as the streamwise, the radial, and the azimuthal RMS velocity fluctuations are presented in Figs. 7(a-d). The profiles are normalized by $u'_0 = 20$ m/sec, which represents the peak value seen in the axial RMS profiles. The experimental data shows some asymmetry in the u_{RMS} profile for both the center planes at the first measurement location. It is noticed that for all three components, the decay and eventual approach to uniform radial profile of Reynolds (normal) stresses as the flow progresses downstream. There are two reasons for this to occur. The first being the mean flow in axial direction eventually approaches uniform radial profile going downstream. And the second reason for uniform (but not zero) RMS profile in all three components is due to the swirling mean flow as seen in Fig. 6(a-d). Overall, the normal Reynolds stress for respective components are in good agreement with the measurements.[4,5]

For comparisons of RMS velocity profiles, we considered only the resolved (or filtered) portion of the fluctuations. And good comparisons with measurements indicates the presence of most of the unsteady motion in the large scale structures which are well resolved and predicted by the LES. These results show that the current LES approach is capable of predicting the mixing region quite accurately. Further comparison with data for the reacting (spray) cases will be reported in the next section.

B. Reacting Simulation

Figure 4 presented time-averaged streamwise velocity along the centerline of the combustor for both non-reacting and reacting simulations. As was observed for the non-reacting case, the axial velocity is consistently negative through the inlet pipe upto the point where the VBB terminates. For the EBULES simulation, there are two locations with negative peak velocity. Both of the values are relatively larger than seen in the non-reacting case. The first peak is located inside the inlet pipe with negative peak value of $0.5U_o$ whereas, the other is located at $x/R_o = 1.5$ with negative $0.28U_o$ peak value. Comparison with the measurements indicate that EBULES underpredicts the strength of the reverse flow region located in the combustor by $0.04U_o$. Also, the placement of the peak is further upstream in EBULES by $0.9R_o$. The rate of gradual increase in the axial velocity past the negative peak location for EBULES is similar to that seen in measurements. The mis-match in the placement of the peak recirculation strength causes the length of the VBB to be under-predicted by $2.1R_o$ for the EBULES. Major cause for this can be attributed to the approximate inflow velocity boundary condition which affects the placement of the flame and eventual volume expansion. Further downstream, the final rate of increase in the axial velocity compares well with the measurements indicating that the overall mass flux and flow conditions are modeled accurately. Preliminary time-averaged centerline axial velocity profile for the LEMLES simulation is also shown. Overall trend for LEMLES simulation is similar to the EBULES. Several ripples are observed along the axial direction indicating insufficient time for statistical convergence.

Figures 8(a,c) show the normalized mean axial velocity profiles in the combustor at various axial locations for two center planes. The experimental data obtained at some of the axial locations are also shown. At the first location, the peak locations in the shear layers are well predicted however, the overall axial velocity profile is under-predicted. This suggests a mis-match in the flame location in part due to assumed inflow

boundary. However, the peak value in the reverse flow region compares well with data suggesting that the bulk flow is captured accurately. Further downstream, with the formation of VBB determined by the combustor geometry, comparison with measurements are in good agreement. This includes the radial spread of the recirculation zone as seen at $x/R_o \approx 2.3$. Axial profiles for the LEMLES simulation are also shown in form of dashed lines. Overall variations are similar to that of EBULES. It is seen from these preliminary LEMLES results that inspite of employing better closure for the species equation, it is unable to correctly predict the flow acceleration at the first measurement location. This directly indicates the necessesity of realistic inflow velocity boundary conditions which can be achieved only by solving through the swirler assembly.

In comparisons with the non-reacting case, the VBB is smaller in both length and width (radial direction) however, the reverse flow is much stronger. The effect of combustion is to increase the overall volume flow rate through the outflow boundary as can be seen by the increase in axial velocity from $0.125U_o$ to $0.352U_o$. It is this property of increased organized (mechanical) energy that is relied upon for extracting work via turbines. Similar to the non-reacting case, the resulting cross-sectional shape of the VBB in the center-planes resembles are leaf with its stem orginating in the inlet pipe. However, in the reacting case, overall size is relatively smaller.

Figures 8(b) and 8(d) show respectively, the normalized mean tangential velocity profiles in the $x - z$ horizontal center-plane, and the radial velocity profiles in the $x - y$ vertical center-plane at various axial locations. For the azimuthal component, both the peak magnitude as well as peak locations in the shear layer regions are well predicted. The radial component, at the first measurement location, shows signs of under-expansion of flow, consistent with axial component. The EBULES shows good trend with measurements but fails to achieve the peak value at the bottom ($r/R_o \approx -1.5$) corner. In comparison, the LEMLES radial profiles are showing better agreement at the top corner and relative improvement in peak radial position in the bottom corner. Elsewhere, the EBULES and LEMLES profiles are similar.

In a similar behavior to non-reacting case, the peak radial velocity rapidly decays moving downstream achieving an uniform profile. It can also be seen that the intensity of the azimuthal velocity is weaker in relation to the radial or axial components however, its decay is not as significant as seen for the radial component. Also, the presence of non-zero variation of azimuthal velocity along various axial locations indicate presence of swirl in the combustor. As was seen in the non-reacting case, the swirl is in the same direction as the outer swirler flow. Keeping in mind the uncertainties relating to inflow boundary and chemical rate closure involved, the characteristics of VBB are reasonably predicted by both approaches.

Comparisons for turbulence properties are presented in Figs. 9(a-d). The profiles are normalized by $u'_0 = 30$ m/sec, which represents the nominal value seen in the axial RMS profiles. The reacting data shows relatively uniform profiles for all three components as compared to the non-reacting RMS profiles, especially at the first measurement location. In the reacting case, the shear layer region, as seen in Fig. 8(a,c) at first axial location, is broadly dispersed in the radial direction amounting to increase turbulence at those locations. Turbulence variations for the LEMLES simulation is seen similar to EBULES. It is noticed that for all three components, the decay and eventual approach to uniform radial profile of Reynolds (normal) stresses as the flow progresses downstream. Except for the first measurement location, the normal Reynolds stress for respective components are in reasonable agreement with the data. At the first location, there is over-prediction in both axial and radial RMS quantities. Origin for this can be traced to the previous inconsistencies seen in axial and radial mean profiles. Overall, the turbulence intensity in the reacting case is $15 - 20\%$ larger than seen in the non-reacting simulation.

Flow visualization for EBULES simulation is shown in Fig. 10(a) in form of streamlines and VBB region. The recirculation regions is seen to be contiguous albeit smaller than seen for the non-reacting case. The streamline patterns are markedly different. Here, the flow is seen not to expand much radially but rather moves downstream at relatively smaller radial angle. This happens due to volume expansion and smaller but stronger recirculation bubble. Viewing the VBB in a cross-sectional plane, as shown in Fig. 10(b), its size in terms of width (radial direction) and length are relatively smaller than the non-reacting case. The flow is also seen to separate at 45^o expansion angle just upstream of the dump plane. Such separation was not observed in the non-reacting simulation. The mean flow is seen to rotate clockwise $\approx \pi$ radians from inflow to the outflow boundary as seen by the streamlines. Rotation is almost half than that noticed in the non-reacting case.

Figure 10(c) shows time-averaged overall fuel reaction rate as solid-colored background super-imposed with mean axial velocity contours in the vertical center-plane. The units for the reaction rate shown are in the CGS system. The overall reaction rate is positioned in the shear layers between the incoming reactants and the recirculation bubble. The reaction rate has contribution from both the mixing (based on turbulence)

and chemical (based on Arrhenius) rates and their breakdown is shown in Fig. 10(d). The mixing rate is limiting in recirculation bubble whereas the chemical rate is limiting in the shear layer region. Also notice that the typical range of mixing rate is approximately 5-10 times the chemical rate. The positioning of the overall flame in the shear layers implies that the recirculating region sustains the flame by providing pool of hot products both for pre-heating the incoming reactants as well as ignition source.

C. Spray Dynamics

Time-averaged fuel particle velocities and SMD profiles are compared to measurements and presented in Fig. 11. All three components of droplet velocities are compared in two center-planes as seen in Fig. 11(a-d). At the first measurement location, velocities profiles compare reasonably well with measurements. Both the peak value, as well as, the peak locations are captured. The droplet axial velocity is seen to peak in the shear layers and follows gas-phase closely. In the center region (around $r/R_o \approx [-0.25, 0.25]$), measurements shows negative axial velocity indicating that the droplets are entrained in the recirculation bubble. LES droplet profile in that region shows positive axial droplet velocity albeit smaller in magnitude. This indicates that incoming droplets are not able to slow down enough to reach negative axial velocity. Several reasons can be attributed to this behavior. Principally, the initial velocity given to the droplets at the inflow boundary is approximated which may be over-specified. Secondly, this study assumes the spray is dilute and no atomization of droplets is taken into account. Presence of small droplets via breakup in the center region would follow gas-phase more accurately. Inspite of these approximations/assumptions, overall trend for droplet velocities is reasonably well predicted.

Sauter-Mean Diameter ($SMD, D32$) profiles are also compared with measurements and presented in Fig. 11(e-f) normalized by nominal value $D_{32,0} = 100\mu m$ seen in measurements. At the first data location, measurements show $D32$ values of $O(100\mu m)$ whereas, the LES is predicting on the range of 30 μm. Colby *et al.*[5] have shown that low fuel injection pressure, as is the case here, could result in poor spray characteristics and off-rated injector performance. The initial droplet distribution given to particles was based in part on rated (at $40\mu m$) SMD of the injector. The mis-match at the first measurement location is expected and seen in the profiles. Further downstream, error in comparisons diminishes in part due to the heat release effects and less influence of nozzle distribution. The heat release, due to droplet evaporation, changes droplet radius distribution, and thereby significantly affecting the SMD profiles. Again, given the approximations employed in this study, overall trend for the particle SMD profiles are reasonably captured especially at downstream locations.

The droplets are seen to follow a hollow cone pattern as seen from both the radial profiles as well as flow visualization (not shown here, for brevity). The trajectory of particles is through the shear layer regions tucked in between the 45^o flare angle and the re-circulation bubble. Then onwards, the particles continue to travel the same trajectory however, at lower velocities until they finally vaporize. The acceleration of particles is seen just upstream of the dump plane in the shear layer regions consistent with gas-phase speedup. Relatively few particles are seen in the recirculation bubble due to longer residence time allowing for complete vaporization. Particles seize to exist past $x/R_o = 3.3$. Closer inspection of SMD profiles indicate that SMD increases both moving radially outwards and downstream axially, consistent with measurements. Lower values of SMD closer to recirculation bubble indicate the effect of proximity of heat source leading to presence of smaller droplets due to rapid particle evaporations. Also, presence of larger particles is seen on the outer periphery owing to their centrifugal acceleration by the gas-phase swirl imparted in the inlet pipe.

VI. Conclusions

Large-Eddy Simulation of swirl-stabilized flow in a laboratory combustor have been performed for non-reacting and reacting conditions and both gas- and liquid-phase results are compared with available data. Methodology employed in this study attempts to capture spray-turbulence interactions as well as subgrid fuel-air mixing and finite rate kinetics. Results for non-reacting case show presence of vortex breakdown bubble (VBB) in the center-line region with two corner recirculation zones past the dump plane. Non-reacting comparisons with measurements for both mean and RMS show good agreement. Reacting simulations show presence of stronger yet smaller VBB in the center-line region. EBULES is seen to under-predict both the location and negative peak value of the axial velocity by $0.9R_o$ and $0.04U_o$, respectively. Overall reacting comparisons with measurements are in reasonable agreement. Time-averaged flow visualization in form of streamlines indicate that the non-reacting flow rotates twice as much from the inflow to outflow boundary

than the reacting case. Droplet data show good agreement for particle velocity profiles and reasonable trends for the SMD variation.

Acknowledgments

This research is supported in part by General Electric Aircraft Engine Company and by NASA/GRC. Computational time provided by NASA/GRC and Computational Combustion Laboratory (CCL) at Georgia-Tech is greatly appreciated.

References

[1]Maclin, H. and Haubert, C., "Fifty Years Down - Fifty Years To Go," *AIAA Paper 2003–2788*, 2003.

[2]Mongia, H. C., "Perspective of Combustion Modelling for Gas Turbine Combustors," *AIAA Paper 2004–0156*, 2004.

[3]Candel, S., Thevenin, D., Darabiha, N., and Veynante, D., "Progress in Numerical Combustion," *Combustion Science and Technology*, Vol. 149, 1999, pp. 297–337.

[4]Colby, J., Jagoda, J., and Menon, S., "Flow Field Measurements in a Swirling Spray Combustor," *AIAA Paper AIAA-2005–4143, 41st Joint Propulsion Conference*, 2005.

[5]Colby, J., Menon, S., and Jagoda, J., "Spray and Emission Characteristics near Lean Blow Out in a Counter-Swirl Stabilized Gas Turbine Combustor," *ASME Turbo Expo 2006; GT2006-90974; Submitted*, 2006.

[6]Tolpadi, A. K., Burrus, D. L., and Lawson, R. J., "Numerical Computation and Validation of Two-Phase Flow Downstream of a Gas Turbine Combustor Dome Swirl Cup," *ASME Journal of Engineering for Gas Turbines and Power*, Vol. 117, 1995, pp. 704–712.

[7]Hsiao, G. and Mongia, H. C., "Swirl Cup Modelling, Part 2: Inlet Boundary Conditions," *AIAA Paper 2003–1350*, 2003.

[8]Hsiao, G. and Mongia, H. C., "Swirl Cup Modelling, Part 3: Grid Independent Solution with Different Turbulence Models," *AIAA Paper 2003–1349*, 2003.

[9]Mongia, H. C., Al-Roub, M., Danis, A., Elliott-Lewis, D., Jeng, S. M. Johnson, A., McDonell, V. G., Smauelsen, G. S., and Vise, S., "Swirl Cup Modelling, Part 1," *AIAA Paper 2001–3576*, 2001.

[10]Wang, S., Yang, V., Mongia, H. C., Hsieh, S. Y., and Hsiao, G., "Modelling of Gas Turbine Swirl Cup Dynamics, Part 5: Large-Eddy Simulation of Cold Flow," *AIAA Paper 2003–0485*, 2003.

[11]Sankaran, V. and Menon, S., "LES of Spray Combustion in Swirling Flows," *Journal of Turbulence*, Vol. 3, 2002, pp. 011.

[12]Menon, S. and Patel, N., "Subgrid Modeling for LES of Spray Combustion in Large-Scale Combustors," *AIAA Journal (in press, 2006)*, 2006.

[13]Kim, W.-W. and Menon, S., "Application of the localized dynamic subgrid-scale model to turbulent wall-bounded flows," *AIAA Paper 97–0210*, 1997.

[14]Kim, W.-W., Menon, S., and Mongia, H. C., "Large-Eddy Simulation of a Gas Turbine Combustor Flow," *Combustion Science and Technology*, Vol. 143, 1999, pp. 25–62.

[15]Chakravarthy, V. K. and Menon, S., "Subgrid Modeling of Premixed Flames in the Flamelet Regime," *Flow, Turbulence and Combustion*, Vol. 65, 2000, pp. 133–161.

[16]Sankaran, V. and Menon, S., "Subgrid Combustion Modeling of 3-D Premixed Flames in the Thin-Reaction-Zone Regime," *Proc. Combust. Inst.*, Vol. 30, 2005, pp. 575–582.

[17]Menon, S., Yeung, P. K., and Kim, W. W., "Effect of subgrid models on the computed interscale energy transfer in isotropic turbulence," *Computers and fluids*, Vol. 25, No. 2, 1996, pp. 165–180.

[18]Kim, W. W., Menon, S., and Mongia, H. C., "Large-Eddy simulation of a gas turbine combustor flow," *Combustion Science and Technology*, Vol. 143, 1999, pp. 25–62.

[19]Menon, S. and Kim, W.-W., "High Reynolds Number Flow Simulations Using the Localized Dynamic Subgrid-Scale Model," *AIAA-96-0425*, 1996.

[20]Menon, S. and Pannala, S., "Subgrid Modeling of Unsteady Two-Phase Turbulent Flows," *AIAA Paper No. 97-3113*, 1997.

[21]Kim, W.-W. and Menon, S., "A New Incompressible Solver for Large-Eddy Simulations," *International Journal of Numerical Fluid Mechanics*, Vol. 31, 1999, pp. 983–1017.

[22]Chakravarthy, V. K. and Menon, S., "Large-Eddy Simulations of Turbulent Premixed Flames in the Flamelet Regime," *Combustion Science and Technology*, Vol. 162, 2000, pp. 175–222.

[23]Chakravarthy, V. K. and Menon, S., "Linear-Eddy Simulations of Reynolds and Schmidt Number Dependencies in Turbulent Scalar Mixing," *Physics of Fluids*, Vol. 13, 2001, pp. 488–499.

[24]Liu, S., Meneveau, C., and Katz, J., "On the Properties of Similarity Subgrid-Scale Models as Deduced from Measurements in a Turbulent Jet," *Journal of Fluid Mechanics*, Vol. 275, 1994, pp. 83–119.

[25]Lilly, D. K., "A Proposed Modification of the Germano Subgrid-Scale Closure Method," *Physics of Fluids A*, Vol. 4, No. 3, 1992, pp. 633–635.

[26]Patel, N., Stone, C., and Menon, S., "Large-Eddy Simulations of Turbulent Flow over an Axisymmetric Hill," *AIAA-03-0967*, 2003.

[27]Germano, M., Piomelli, U., Moin, P., and Cabot, W. H., "A Dynamic Subgrid-Scale Eddy viscosity Model," *Physics of Fluids A*, Vol. 3, No. 11, 1991, pp. 1760–1765.

[28]Schumann, U., "Realizability of Reynolds-Stress Turbulence Models," *Physics of Fluids*, Vol. 20, No. 5, 1977, pp. 721–725.

[29]Fureby, C. and Möller, S.-I., "Large-Eddy Simulation of Reacting Flows Applied to Bluff Body Stabilized Flames," *AIAA Journal*, Vol. 33, No. 12, 1995, pp. 2339–2347.

[30]Kerstein, A. R., "Linear-Eddy Model of Turbulent Transport: Part 2," *Combustion and Flame*, Vol. 75, 1989, pp. 397–413.

[31]Menon, S. and Kerstein, A. R., "Stochastic Simulation of the Structure and Propagation Rate of Turbulent Premixed Flames," *Proc. Combust. Inst.*, Vol. 24, 1992, pp. 443–450.

[32]Menon, S., McMurtry, P., and Kerstein, A. R., "A Linear Eddy Mixing Model for Large Eddy Simulation of Turbulent Combustion," *LES of Complex Engineering and Geophysical Flows*, edited by B. Galperin and S. Orszag, Cambridge University Press, 1993, pp. 287–314.

[33]Menon, S. and Calhoon, W., "Subgrid Mixing and Molecular Transport Modeling for Large-Eddy Simulations of Turbulent Reacting Flows," *Proc. Combust. Inst.*, Vol. 26, 1996, pp. 59–66.

[34]Pope, S. B., "PDF Methods for Turbulent Reactive Flows," *Progress in Energy and Combustion Science*, 1985, pp. 119–192.

[35]Oefelein, J. C. and Yang, V., "Simulation of High-Pressure Spray Field Dynamics," *Recent Advances in Spray Combustion:Spray Combustion and Droplet Burning Phenomena, Progress in Astronautics and Aeronautics*, Vol. 166, 1995, pp. 263–304.

[36]Faeth, G. M., "Mixing, Transport and Combustion in Sprays," *Progress in Energy and Combustion Science*, Vol. 13, 1987, pp. 293–345.

[37]Crowe, C. T., Sommerfeld, M., and Tsuji, Y., "Multiphase Flows with Droplets and Particles," CRC Press LLC, Boca Raton, FL, 1998.

[38]Faeth, G. M., "Evaporation and combustion of sprays," *Progress in Energy and Combustion Science*, Vol. 9, 1983, pp. 1–76.

[39]Chen, K. H. and Shuen, J. S., "A coupled Multi-block solution procedure for spray combustion in complex geometries," *AIAA Paper 1993-0108*, 1993.

[40]Reid, R. C., Prausniz, J. M., and Poling, B. E., Mcgraw Hill Publishing Company, 1988.

[41]Sankaran, V., "Sub-grid combustion modeling for compressible two-phase flows," Doctorate Thesis, Georgia Inst. of Technology, Aerospace Eng., 2003.

[42]Westbrook, C. K. and Dryer, F. L., "Simplified Reaction Mechanisms for the Oxidation of Hydrocarbon Fuels in Flames," *Combustion Science and Technology*, Vol. 27, 1981, pp. 31–43.

[43]Malte, P., Hamer, A., Roby, R., and Steele, R., "Development of a Five-Step Global Methane Oxidation-NO Formation Mechanism for Lean-Premixed Gas Turbine Combustion," *Trans. of the ASME: J. of Eng. for Gas Turbine and Power*, Vol. 121, No. April, 1999, pp. 272–280.

[44]Fureby, C. and Löfström, C., "Large-Eddy Simulations of Bluff Body Stabilized Flames," *Proc. Combust. Inst.*, Vol. 25, 1994, pp. 1257–1264.

[45]Stone, C. and Menon, S., "Adaptive swirl control of combustion instability in gas turbine combustors," *Proc. Combust. Inst.*, Vol. 29, 2002, pp. 155–160.

[46]Poinsot, T. and Lele, S., "Boundary Conditions for Direct Simulations of Compressible Viscous Flow," *Journal of Computational Physics*, Vol. 101, 1992, pp. 104–129.

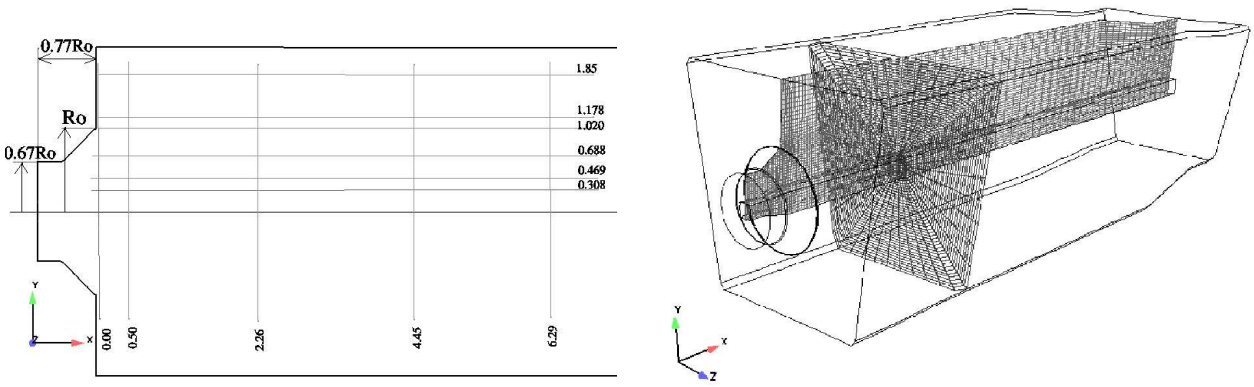

(a) Schematic

(b) Computational Grid

Figure 1. Computational domain for the combustor; outer cylindrical grid: 185×74×81 and inner cartesian grid: 185×21×21. Schematic of the grid is shown along with probe locations (at intersection of thin lines) at which transient signals are collected. Numbers represent distances (x/R_o, r/R_o) for the probes from the dump plane and combustor center-line, respectively.

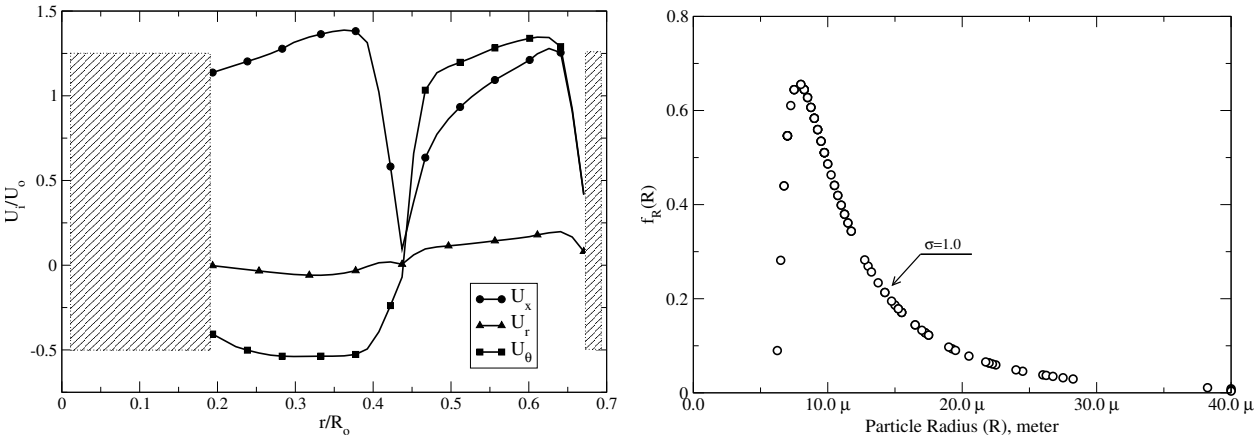

(a) Inflow Profiles

(b) Particle Size Distribution

Figure 2. Velocity inflow profiles (U_x, U_r, U_θ) normalized by the bulk flow velocity (U_o) used for the simulations are shown in (a). For droplets, a log-normal size distribution is used with a SMD of 31.2 μm.

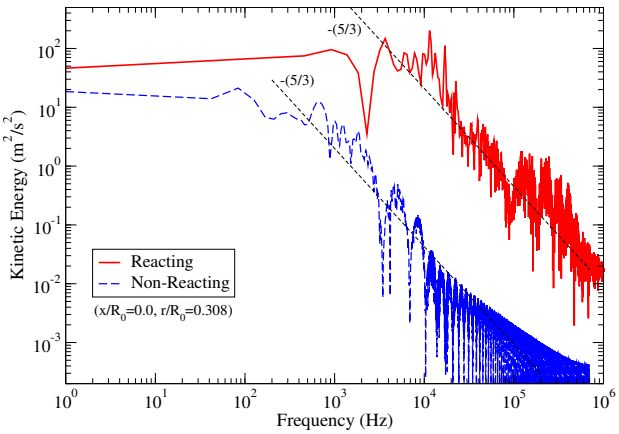

Figure 3. Kinetic energy spectrum for both the reacting and non-reacting case showing the $(-5/3)$ slope for decay of energy indicating attainment of inertial layer using the current grid. Probe location for the spectrum is in the shear layer region just downstream of the dump plane.

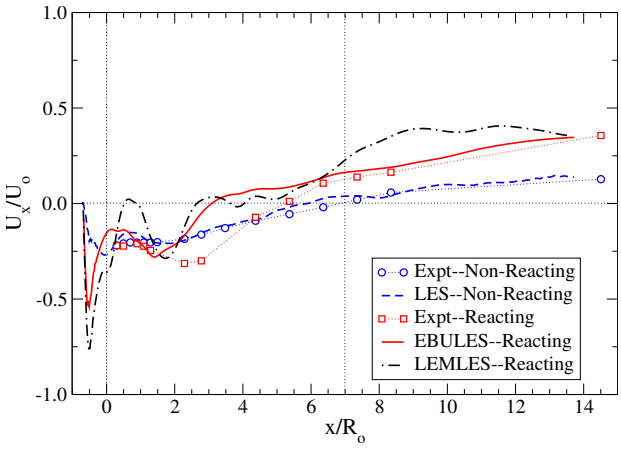

Figure 4. Time-averaged centerline streamwise non-dimensional velocities for the non-reacting and reacting cases are shown. Parameters used for non-dimensionalization are the bulk velocity (U_o) and dump plane expansion radius (R_o).

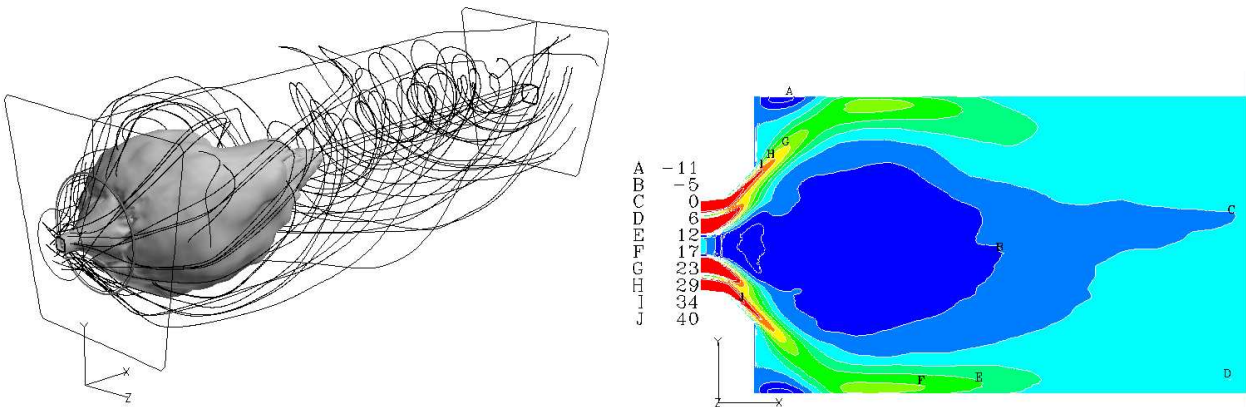

(a) Non-Reacting VBB

(b) Non-Reacting $X - Y$ Plane

Figure 5. Time-averaged axial velocity iso-surface at zero velocity depicting VBB is shown in (a) for non-reacting case. Also shown are streamlines originating from the inflow boundary. Mean axial velocity contours in the horizontal plane are shown in (b) showing the cross-section as a *leaf* shaped structure.

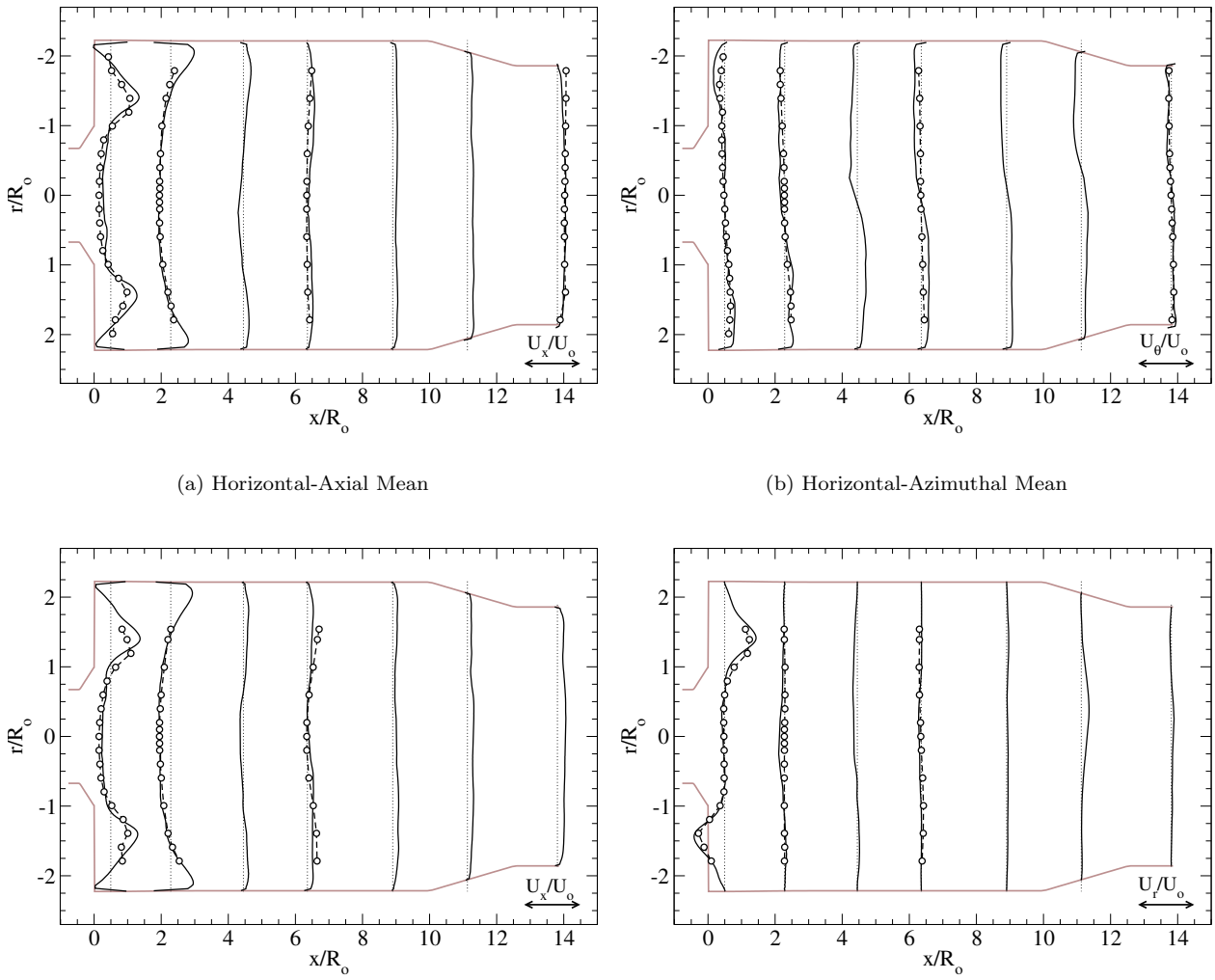

(a) Horizontal-Axial Mean

(b) Horizontal-Azimuthal Mean

(c) Vertical-Axial Mean

(d) Vertical-Radial Mean

Figure 6. Time-averaged horizontal ($X-Z$) and vertical ($X-Y$) plane comparisons for non-reacting simulations. Open symbols represent measurement data points. Scaling used for non-dimensionalization is the bulk flow velocity (U_o) and the dump expansion radius (R_o) or as noted in the discussion.

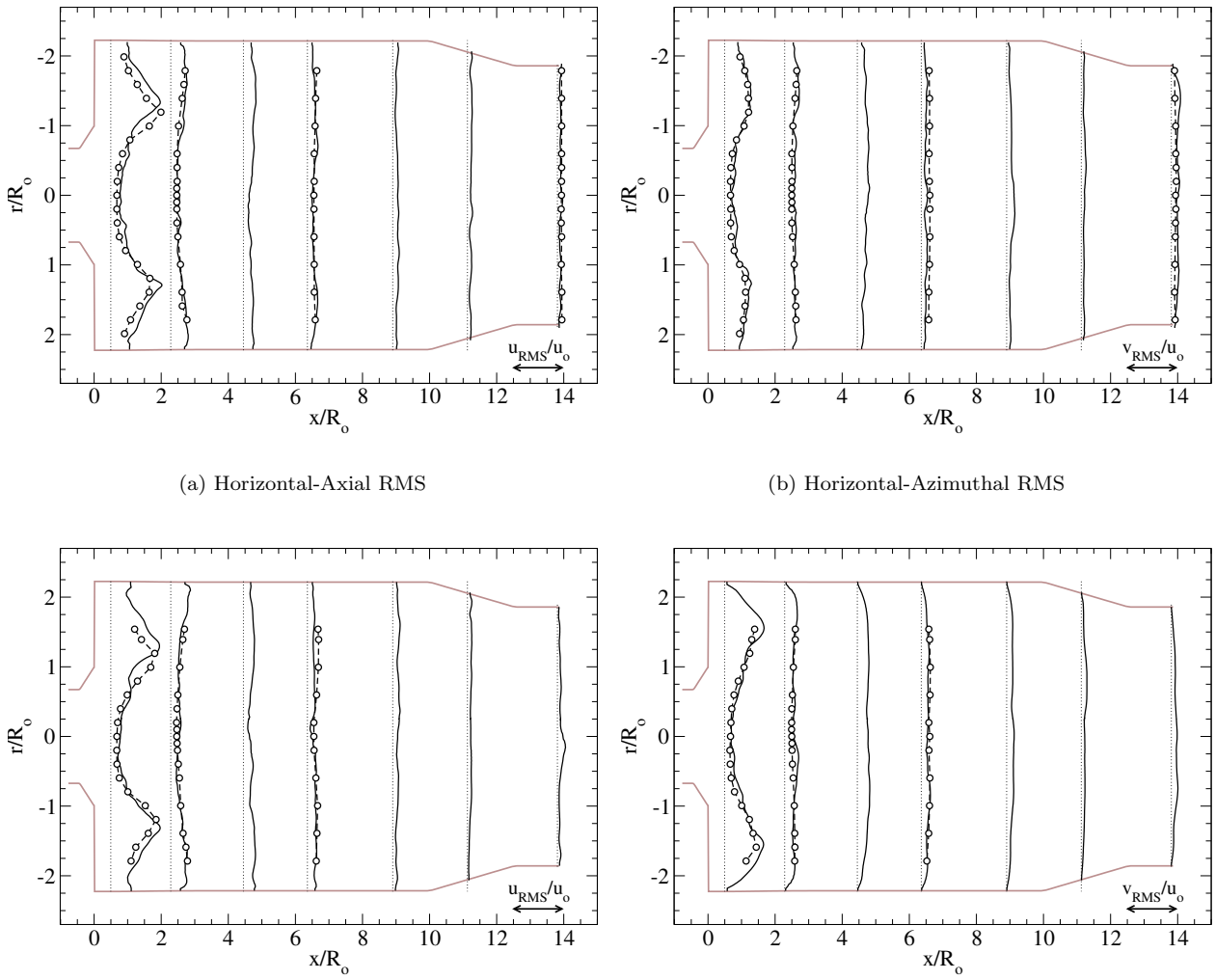

(a) Horizontal-Axial RMS

(b) Horizontal-Azimuthal RMS

(c) Vertical-Axial RMS

(d) Vertical-Radial RMS

Figure 7. Time-averaged horizontal ($X-Z$) and vertical plane ($X-Y$) comparisons for non-reacting simulations. Open symbols represent measurement data points. Scaling used for non-dimensionalization is the bulk flow velocity (U_o) and the dump expansion radius (R_o) or as noted in the discussion.

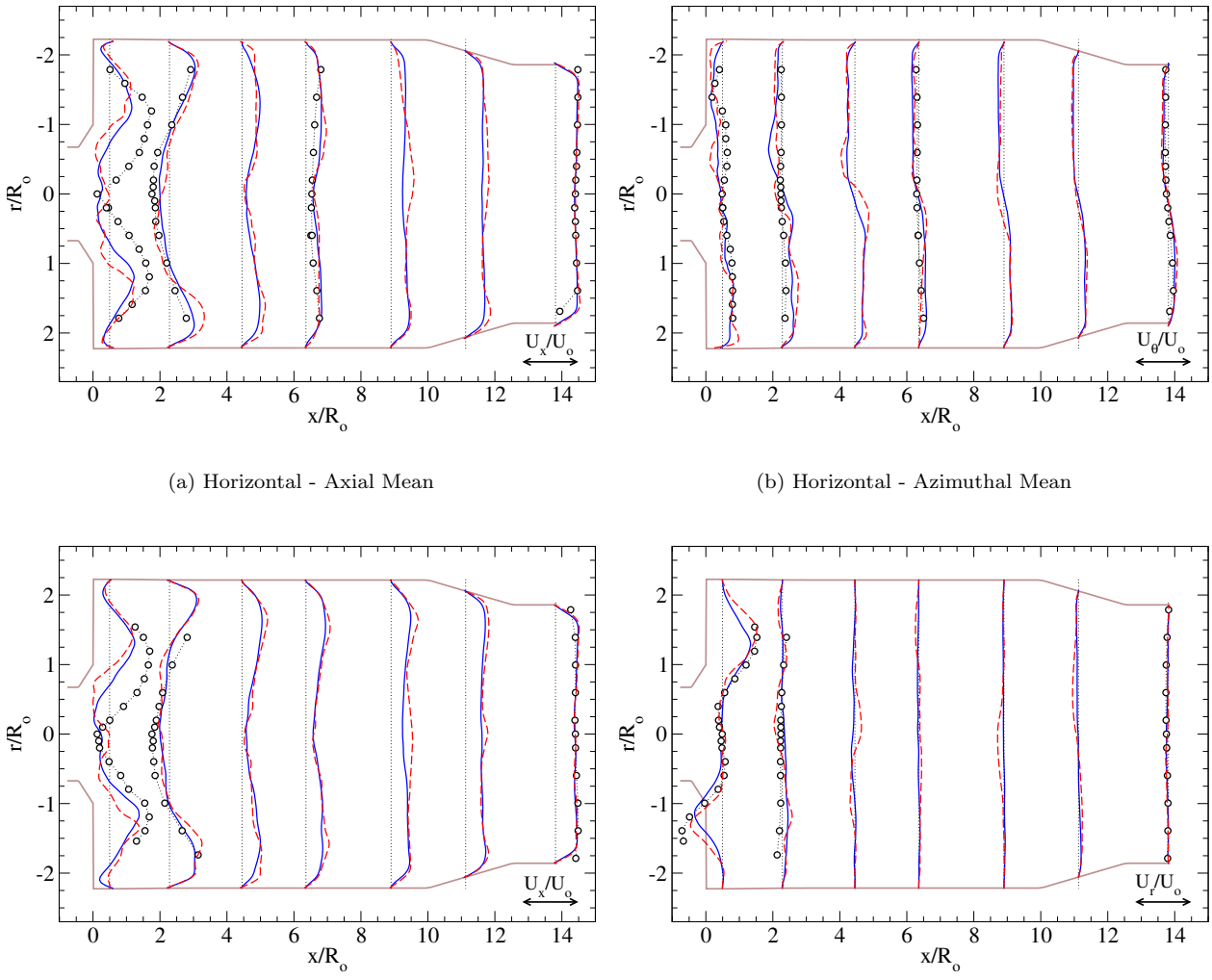

(a) Horizontal - Axial Mean

(b) Horizontal - Azimuthal Mean

(c) Vertical - Axial Mean

(d) Vertical - Radial Mean

Figure 8. Time-averaged horizontal ($X-Z$) and vertical ($X-Y$) plane comparisons for reacting simulations. Open symbols represent measurement data points. Scaling used for non-dimensionalization is the bulk flow velocity (U_o) and the dump expansion radius (R_o). Solid blue lines represent EBULES and red dashed lines are for LEMLES simulations.

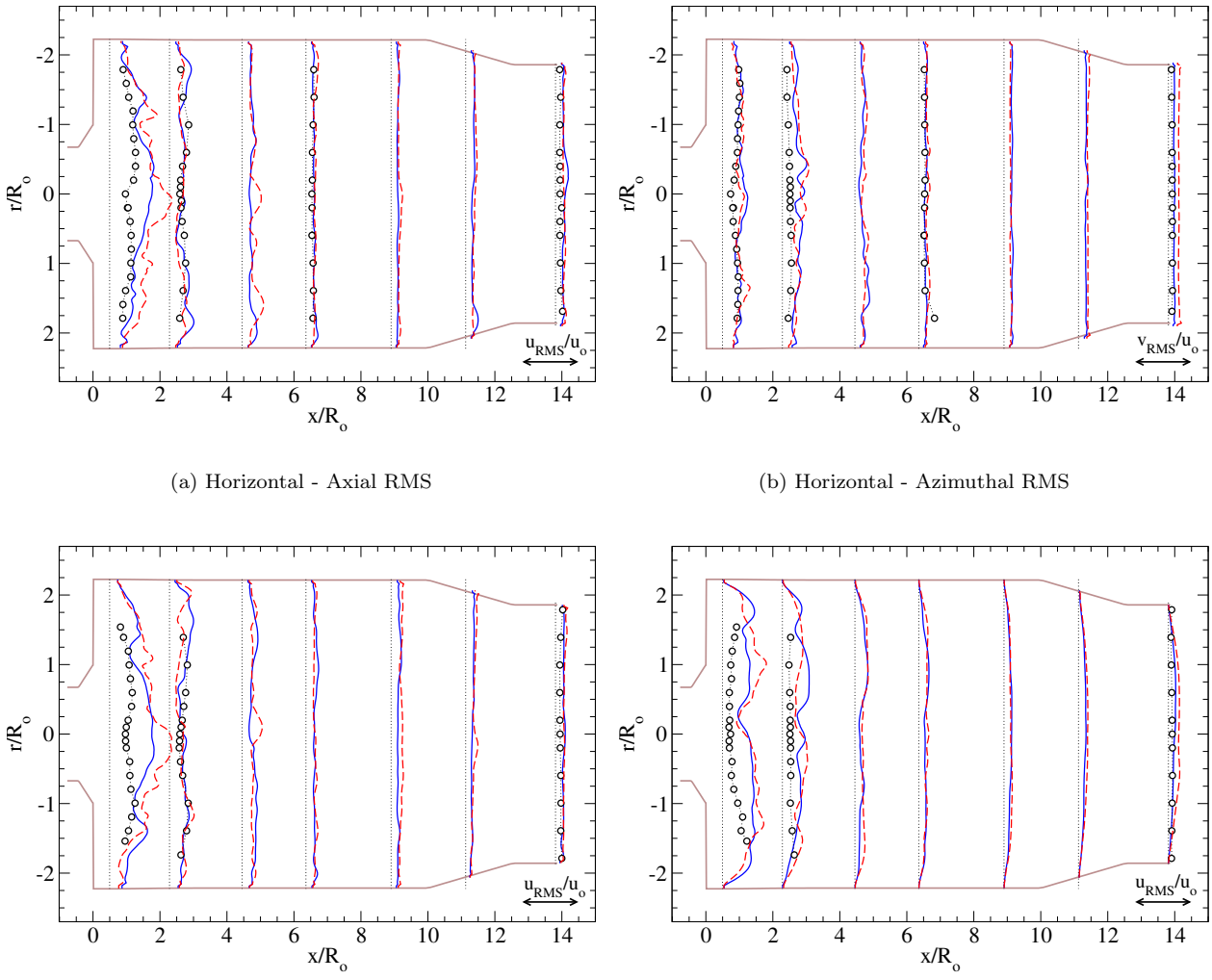

(a) Horizontal - Axial RMS

(b) Horizontal - Azimuthal RMS

(c) Vertical - Axial RMS

(d) Vertical - Radial RMS

Figure 9. Time-averaged horizontal ($X - Z$) and vertical ($X - Y$) plane RMS comparisons for reacting simulations. Open symbols represent measurement data points. Scaling used for non-dimensionalization is the nominal axial RMS velocity (u_o) and the dump expansion radius (R_o). Solid blue lines represent EBULES and red dashed lines are for LEMLES simulations.

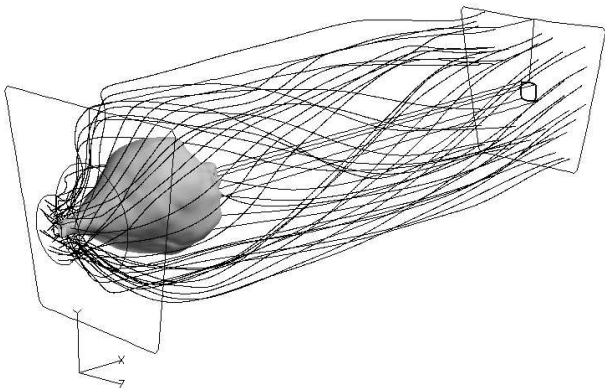

(a) Reacting VBB

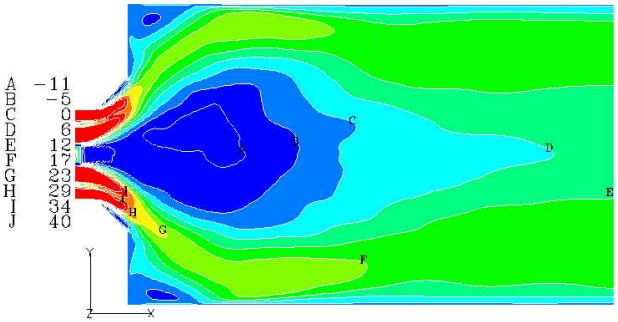

(b) Reacting $X - Y$ Plane

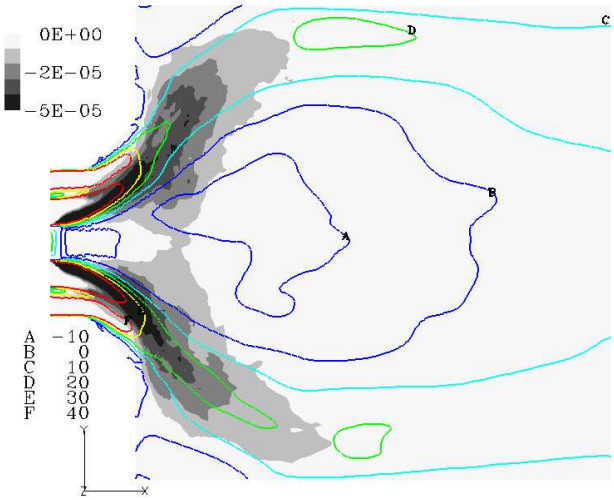

(c) Fuel Reaction Rate

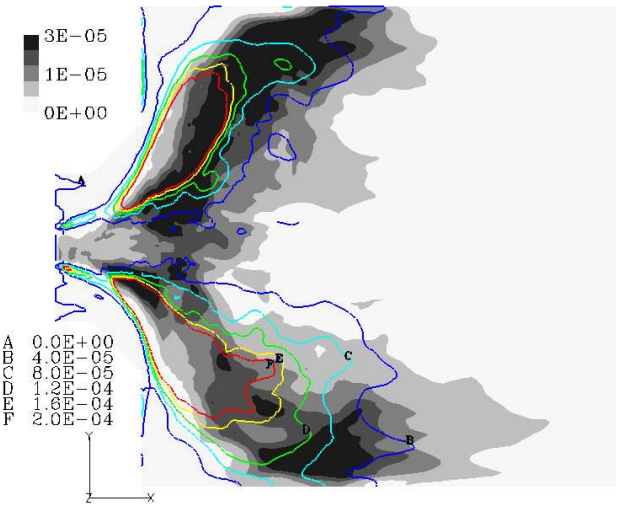

(d) Mixing and Chemical Rate

Figure 10. Time-averaged axial velocity iso-surface at zero velocity depicting VBB is shown in (a). Also shown are streamlines for the EBULES simulation. Mean axial velocity contours in the horizontal plane are shown in (b). Time-averaged fuel reaction rate (as solid contours) in the horizontal plane with axial velocity line contours is shown in (c) for EBULES simulation. Mixing (as line contours) and chemical rate (as solid contours) contributing to overall fuel reacting rate are shown in (d). Reaction rates are in CGS units.

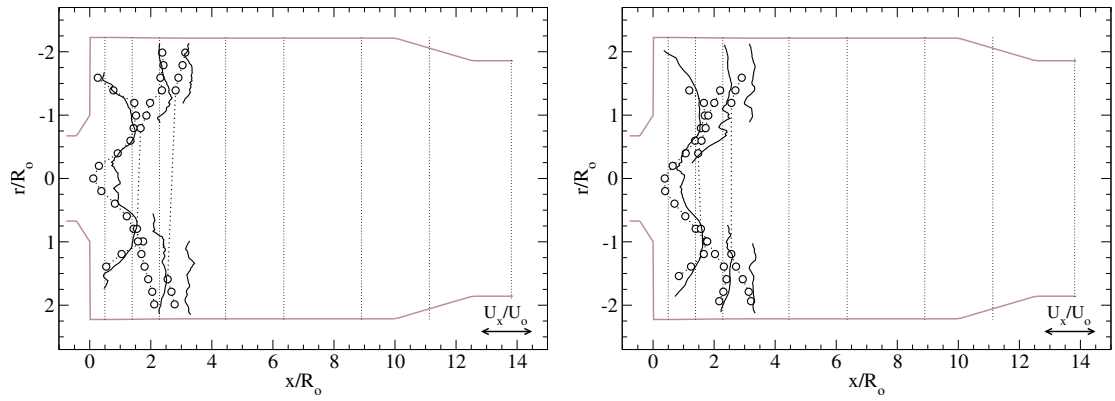

(a) Horizontal - Axial Mean

(b) Vertical - Axial Mean

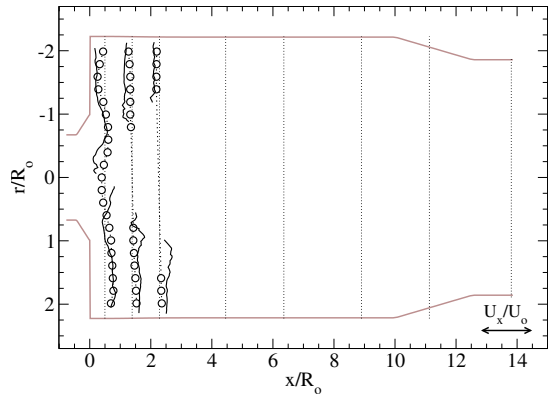

(c) Horizontal - Azimuthal Mean

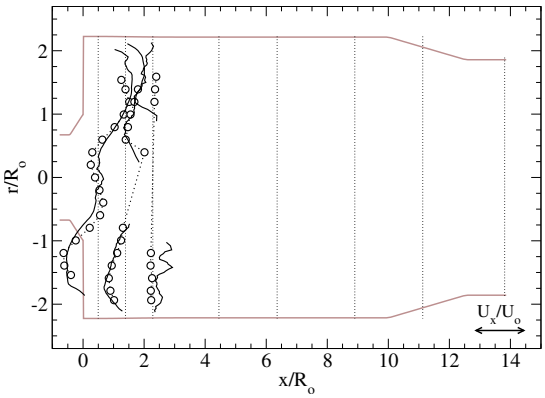

(d) Vertical - Radial Mean

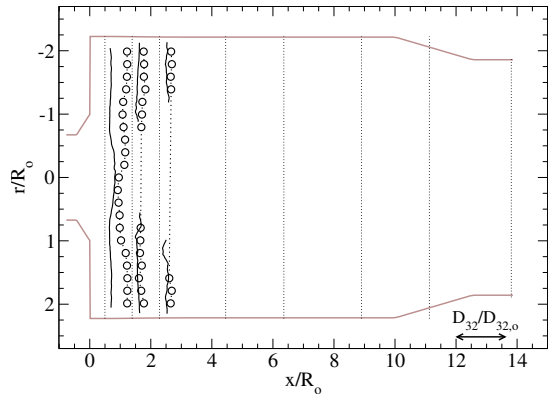

(e) Horizontal - D32 Mean

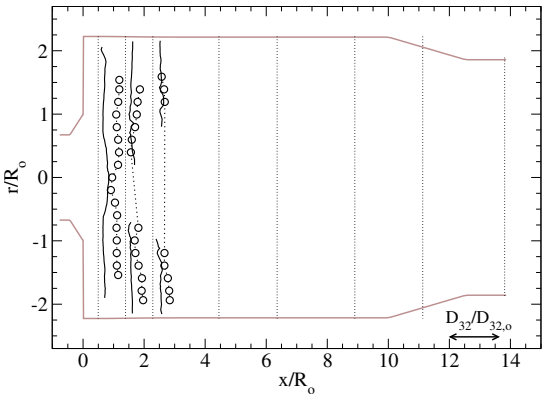

(f) Vertical - D32 Mean

Figure 11. Time-averaged horizontal ($X-Z$) and vertical ($X-Y$) plane droplet comparisons for reacting EBULES simulation.